Converged three-dimensional calculations of above-threshold ionization: Angular-momentum constraints and the kinetic-energy distribution

Ricardo A. Blank and Moshe Shapiro
Chemical Physics Department, Weizmann Institute of Science, Rehovot 76100, Israel
(Received 28 February 1994)

We present an application of the artificial-channel method to the calculation of multiphoton ionization rates under continuous-wave illumination conditions. We use the method to treat above-threshold ionization (ATI) of hydrogen in three dimensions with linearly and circularly polarized light at field intensities ranging from 10^9 to 10^{14} W/cm^2. The results are compared with perturbative as well as nonperturbative calculations for short pulses and with experiments. The range of validity of the dipole approximation for ATI processes is also examined. An analysis of both the angular and angular-momentum distribution of the photoelectrons at different intensities is presented. We find that ATI cross sections for circularly polarized light at 532 nm are three orders of magnitude weaker, with electronic kinetic energies peaking at higher values, than in the case of linearly polarized light. This last effect is shown to result from the different ponderomotive potential experienced by the electron, due to the drastically different angular distributions computed for the two cases. Connection is made between the angular distributions, and the angular-momentum constraints affecting it, and the kinetic energy of the ensuing electrons. It is argued that it is difficult to understand the ATI process without taking the three-dimensional aspects of the problem into consideration.

PACS number(s): 32.80.Rm, 42.50.Hz

I. INTRODUCTION

Above-threshold ionization (ATI) consists of the absorption of a (large) number of photons in the continuous part of an atomic spectrum. In this paper we analyze the ATI problem by solving the Schrödinger equation for an electron under the simultaneous action of the atomic and laser fields. This is done for a number of reasons. First, since both fields can be strong, perturbative methods and most other approximate methods are expected to fail. Whereas many models seem to explain qualitatively well the distribution of the kinetic energy ("ATI peaks") of the ensuing electron(s), the direct solution of the Schrödinger equation is required if one wants to study the dependence of the process on the photon energy. This is especially so with respect to the possible effect of intermediate atomic bound states, which broaden and shift in a nontrivial way under the action of the intense laser field.

There are additional reasons for a full numerical study of the problem in three dimensions (3D). Currently, the prevailing feeling is that in order to understand the kinetic-energy distribution of the ATI electrons, it is sufficient to follow the electron from the instant it enters the continuum [1–4]. There is, however, evidence based on a comparison with experiments [5] and accurate numerical simulations [6], that reveals substantial quantitative discrepancies with the above models. Below, we show that the manner in which the electron enters the continuum is important. In particular, we show that the kinetic-energy distribution is affected by the number and angular momenta of the photons absorbed as the system makes its way to the final continuum level.

In the past a number of studies have, in fact, included both the bound-continuum and continuum-continuum aspects of the problem. However, often a number of simplifying assumptions were made. Thus, when it was felt that the contribution of intermediate resonances could be ignored, the bound-continuum part of the process was treated using Nth-order perturbation theory [7,8], where N is the number of photons needed to reach the continuum. Although perturbation theory works well for weak fields, it fails for strong fields. Alternatively, models in which only a truncated number of (bound and continuum) "essential states," generally chosen to be in resonance with some integer multiple of the photon energy, have been employed [9–12]. The essential-states-type models fail, however, for really strong fields that induce strong mixing between highly off-resonance (bound and continuum) levels.

A different philosophy was to solve the problem fully using model potentials [13–15] embedded in some cases in a reduced number (one or two) of dimensions [14,16]. The choice of model potentials is often dictated by a desire to overcome the singularity at the origin and the very long-range aspect of the Coulomb and radiative interactions. This is done by adding reflecting [14] or absorbing [15,17] potentials at well chosen boundaries or by choosing periodic potentials [18].

As we show below, there are salient features of the process which are only manifest in the 3D world. This is particularly so with respect to the influence of the electron's angular momenta on the effective field driving the electron. We show that the angular-momentum distribution affects the average ponderomotive potential, which, in turn, affects the electronic kinetic-energy distribution. Since different polarizations impose different angular-momentum constraints, the 3D aspects of the

process are important for understanding the kinetic-energy distribution of the ATI electrons.

What hampers the execution of accurate calculations in 3D is mainly the long-range nature of the Coulomb and radiation-matter interactions. In particular, if one works in the (otherwise convenient) length form, the radiation-matter interaction, $\mu\cdot\mathcal{E}$ (the electric dipole times the field), may extend literally over macroscopic sizes. This problem is not so severe when short pulses (lasting 10–50 fsec) are considered. Schafer and Kulander [19] have solved directly the time-dependent Schrödinger equation for such pulses. In this case, the radiation-matter interaction shuts off before the electron can travel too far. As a result, the spatial integration can be stopped after a few hundred Å or less.

Many of the ATI experiments [5,20,21] are, however, conducted with nsec or psec pulses, which subject the electron to strong interactions over many thousands of Å. Under these circumstances the direct solution of the time-dependent Schrödinger equation is impossible. Even the solution of the time-independent Schrödinger equation is difficult. In the past, the problem has been dealt with within the framework of Floquet theory [22–24], where an eigenvalue matrix equation is solved. The solutions are the complex energy values of the dressed laser-atom eigenstates whose imaginary part gives the total rate of ionization from each state. There are different versions of the Floquet method. Recently, alternative methods that combine the formalisms of R-matrix and Floquet theory for solving multiphoton ionization problems have been developed [24]. In this method the R matrix is propagated from an internal region (close to the nucleus) to an external one (far from the nucleus) where the eigenvalue problem for the dressed states is solved.

In this paper we present an efficient algorithm which allows for the direct evaluation of the steady-state ionization rates from an initial bound state to the various final kinetic-energy states. This is done by propagating the (r-dependence) matter-field coupled-channels (CC) equations from the neighborhood of the nucleus up to the "detector zone" where the field is absent, and imposing there the bound-continuum boundary conditions via the use of the artificial-channel method (ACM) [25]. In this way, we are able to consider the multiple absorption of photons in the bound and continuum manifolds in a uniform way. Since the bound-state manifold is an integral part of the calculations, the effect of resonances derived from the remnants of the atomic bound states is automatically taken into account.

We present full 3D computations of the ATI of hydrogen by 532-nm cw light. We also test the validity of the dipole approximation at the large electron-proton separations typical of this problem. We compare our results with other perturbative [7] and ultrashort-pulse [19] studies, as well as with experiments [21]. We examine intensities ranging from "weak" ($I=10^9$ W/cm^2) to "strong" ($I=10^{14}$ W/cm^2), for linear, as well as circular, polarizations. The latter computation constitutes the first full numerical study of this case. We show that the angular and angular-momentum distributions are connected to the observed kinetic-energy distribution. This connection is made via the computation of the dependence of the average ponderomotive potential (AC stark shift) on the electronic angular distribution.

II. METHOD

The derivation of our working equations for the strong-field ionization rate of an atom subjected to a cw radiation field proceeds as follows. We consider the case in which we adiabatically switch on the radiation-matter interaction,

$$V=-\mu\cdot\mathcal{E}\ , \tag{1}$$

where μ is the dipole operator and $\mathcal{E}$ is the radiation electric field. Under these conditions, the steady-state photoionization rate is given [26] as

$$R(E,l,m,n|E_i,l_i,m_i,n_i) = 2\pi|A(E,l,m,n|E_i,l_i,m_i,n_i)|^2\delta(E+n\omega-E_i-n_i\omega)\ , \tag{2}$$

where a.u. are used throughout this paper. $A(E,l,m,n|E_i,l_i,m_i,n_i)$—the photoionization amplitudes—is given as

$$A(E,l,m,n|E_i,l_i,m_i,n_i) = \langle(E,l,m,n)^-|V|E_i,l_i,m_i\rangle|n_i\rangle\ . \tag{3}$$

In the above, $|E_i,l_i,m_i\rangle|n_i\rangle$ is the initial state which is assumed to be the product of bound material state (e.g., the hydrogenic 1s state) and a radiation state with n_i photons in a single radiation mode of frequency ω. $|E_i,l_i,m_i\rangle|n_i\rangle$ is therefore the eigenstate of the *noninteracting* Hamiltonian

$$H_0=H_M+H_{\rm rad}\ , \tag{4}$$

where H_M is the material Hamiltonian and $H_{\rm rad}$ is the radiative Hamiltonian. The noninteracting Hamiltonian has both bound,

$$H_0|E_i,l_i,m_i\rangle|n_i\rangle = (E_i+n_i\omega)|E_i,l_i,m_i\rangle|n_i\rangle\quad(E_i<0)\ , \tag{5}$$

and continuum,

$$H_0|E,l,m\rangle|n\rangle=(E+n\omega)|E,l,m\rangle|n\rangle\quad(E>0)\ . \tag{6}$$

states.

$|(E,l,m,n)^-\rangle$ of Eq. (3) is an eigenstate of the fully interacting Hamiltonian $H(H=H_0+V)$

$$H|(E,l,m,n)^-\rangle=(E+n\omega)|(E,l,m,n)^-\rangle\ . \tag{7}$$

It is the *incoming* scattering solution (a "minus" state), i.e., it correlates in the distant future (as the radiative interaction V is switched off) with $|E,l,m\rangle|n\rangle$—*one* of the noninteracting continuum eigenstate of H_0. In order to calculate the photoionization amplitude of Eq. (3), we first expand $|(E,l,m,n)^-\rangle$ in the eigenstates of the angular-momentum operator $|l,m\rangle$ and the photon occupation number states $|n\rangle$,

$$\langle R|(E,l,m,n)^-\rangle=\frac{1}{R}\sum_{\nu'}\psi^{\nu}_{\nu'}(R)|\nu'\rangle\ , \tag{8}$$

where $\nu\equiv\{l,m,n\}$ and $|\nu\rangle\equiv|l,m,n\rangle$.

The radial-channel wave functions $\psi^{\nu}_{\nu'}(R)$ are obtained by substituting Eq. (8) into Eq. (7) and projecting onto each $|\nu\rangle$ state. The result is a set of CC equations,

$$\left[E_i+(n_i-n)\omega+\frac{1}{2m_e}\frac{d^2}{dR^2}-\frac{l(l+1)}{2m_eR^2}+\frac{1}{R}\right]\psi_{\nu}=\sum_{\nu'}D_{\nu,\nu'}\psi_{\nu'}\ , \tag{9}$$

where m_e is the electron-proton reduced mass and

$$D_{\nu,\nu'}=\langle n|\langle l,m|V|l',m'\rangle|n'\rangle\ . \tag{10}$$

The form of this matrix is dictated by the coordinate dependence of V, which is written explicitly as,

$$V=-\boldsymbol{\mu}\cdot\boldsymbol{\mathcal{E}}=ie\sum_k\left[\frac{2\pi\omega_k}{v}\right]^{1/2}\mathbf{R}\cdot\hat{\boldsymbol{\varepsilon}}_{\mathbf{k}}[a_k^{\dagger}\exp(-i\mathbf{k}\cdot\mathbf{R})-a_k\exp(i\mathbf{k}\cdot\mathbf{R})]\mho\ , \tag{11}$$

where e is the electronic charge, v is the cavity volume. ε_k and ω_k are, respectively, the polarization vector and angular frequency of the k mode, and

$$\mho=\exp\left[-\left[\frac{R}{\alpha}\right]^2\right] \tag{12}$$

models the transverse spatial profile of the laser.

Because the initial state in the photoionization problem is a bound state and the final state is a continuum state [see Eq (3)], this type of problem is sometimes called a "half-collision" problem. The artificial-channel method [25] allows one to transform any half-collision problem into an ordinary *full*-collision ("scattering") problem (in which both initial and final states are in the continuum). In this way, it is possible to solve half-collision problems using the arsenal of numerical methods available for multichannel scattering. In the present application, the propagation of the CC equations is done with the Manolopoulos modification [27] of Johnson's log-derivative algorithm [28].

The essence of the ACM is the addition of one ("artificial") channel to the set of "physical" channels. The artificial channel is used to inject particle flux into the manifold of bound initial states. The coupling between the artificial channel and the bound manifold is introduced in a unidirectional way (back transitions are not allowed) so as to properly maintain the bound-state nature of the initial states. This nonsymmetric coupling gives rise to a nonunitary S matrix, which was shown [25] to possess simple poles, lying on the real axis, whose positions correspond to the exact bound-state energies and whose residues correspond to the desired bound-free transition amplitudes.

The equations solved in the ACM for the hydrogenic ATI problem assume the following form: The P (physical) manifold

$$\left[E-n\omega+\frac{1}{2m_e}\frac{d^2}{dR^2}-\frac{l(1+1)}{2m_eR^2}+\frac{1}{R}\right]F_{\nu}(R)-\sum_{\nu'}D_{\nu,\nu'}(R)F_{\nu'}(R)=D_{\nu,b}(R)F_b(R)\ , \tag{13}$$

coupled to an initial bound subspace

$$\left[E-n_i\omega+\frac{1}{2m_e}\frac{d^2}{dR^2}-\frac{l_i(l_i+1)}{2m_eR^2}+\frac{1}{R}\right]F_b(R)=W_{ba}(R)F_a(R)\ , \tag{14}$$

which, in turn, is coupled to an artificial channel

$$\left[E-\epsilon_a+\frac{1}{2m_e}\frac{d^2}{dR^2}-W_{aa}(R)\right]F_a(R)=0\ . \tag{15}$$

In the above, $E=E_i+n_i\omega$.

As explained below, the results for the final bound-free matrix elements are insensitive to the exact form of the artificial-channel asymptotic energy ϵ_a and the artificial-channel potentials $W_{aa}(R)$ and $W_{ba}(R)$ [29].

Equations (13)–(15) can be written more compactly in matrix notation as

$$\left\{\left[E+\frac{1}{2m_e}\frac{d^2}{dR^2}\right]\mathbf{I}-\mathbf{V}(R)\right\}\mathbf{F}(R)=0\ , \tag{16}$$

where the potential matrix is of the form

$$\mathbf{V}(R)=\begin{bmatrix}W_{aa}(R)+\epsilon^a & O^{\dagger} & 0\\ O & \mathbf{D}(R)+\hat{\mathbf{n}}\omega & D_b(R)\\ W_{ba}(R) & O^{\dagger} & V_b(R)+n_i\omega\end{bmatrix}, \tag{17}$$

where $\hat{n}$ is a diagonal matrix of photon occupation numbers. The matrix of solution is of the form

$$\mathbf{F}(R)=\begin{bmatrix}F_a^a & O^{\dagger} & 0\\ F_P^a & \mathbf{F}_P^P & F_P^b\\ F_b^a & F_b^P & F_b^b\end{bmatrix}. \tag{18}$$

In the above, bold-type symbols represent rectangular submatrices, italic-type symbols represent column vectors, and † represents a Hermitean adjoint (for real matrices, a matrix transpose). For example, **O**, O, and $O^{\dagger}$ denote zero rectangular matrix, zero column vector, and zero row vector, respectively.

The **S** matrix derived from Eqs. (16) can be obtained using a variety of multichannel propagation schemes [28,27]. Of greatest interest to us are the **S**-matrix elements linking the artificial channel to the physical space, which can be written, using standard expressions as

$$S_{\nu,a}(E)=2\pi\langle\mathbf{E},\nu^-|D|\mathbf{F}_b^{+a}(E)\rangle\ , \tag{19}$$

with $\langle\mathbf{E},\nu^-|$ being the (incoming) physical solutions. It can be shown [25,26] that with the special nonsymmetric form of Eqs. (16) the above matrix elements become

$$S_{\nu,a}(E)=2\pi i\sum_n\frac{\langle\mathbf{E},\nu^-|D|E_n\rangle\langle E_n|W_{ba}|F_a^{+a}(E)\rangle}{E-E_n}\ , \tag{20}$$

where E_n and $|E_n\rangle$ are the bound eigenenergies and eigenstates of noninteracting Hamiltonian [Eq. (5)].

It follows from Eq. (20) that all the $S_{v,a}$ matrix elements have poles at E_n—the bound-state energies of the noninteracting Hamiltonian. The *residues* of these poles are directly related to the desired radiative transition amplitudes

$$f_{v,n}(E)\equiv\langle E,v^-|D|E_n\rangle=\frac{1}{2\pi i}\mathrm{Res}_n\left\{\frac{S_{v,a}(E)}{A_n(E)}\right\}, \quad (21)$$

where

$$A_n(E)=\langle E_n|W_{ba}|F_a^{+a}(E)\rangle\ . \quad (22)$$

The quantity A_n and the bound-state energies E_n are most conveniently calculated in a separate smaller calculation in which the whole P manifold is replaced by a second artificial channel a' whose $W_{a'a'}$ channel potential and $W_{a'b}$ coupling term (a' is coupled to the bound manifold) are set identical to W_{aa} and W_{ba}. The $S_{a',a}$ matrix element resulting from this set of equations, which is identical in structure to Eq. (16), is of the form

$$S_{a',a}(E)=2\pi i\sum_n\frac{\langle F_{a'}^{a'-}(E)|W_{ba}|E_n\rangle\langle E_n^\dagger|W_{ba}|F_a^{a+}(E)\rangle}{E-E_n}$$

$$=2\pi i\exp(2i\delta_a)\sum_n|A_n(E)|^2/(E-E_n)\ . \quad (23)$$

Hence, $|A_n(E=E_n)|^2$ are obtained as

$$|A_n(E_n)|^2=\left|\frac{1}{2\pi}\mathrm{Res}_{n'}S_{a',a}(E)\right|, \quad (24)$$

and E_n are obtained as the corresponding pole positions. These poles can be located very efficiently [30] using only a few iterations (see Appendix A of Ref. [30]). Typically [31], an eigenvalue can be located to an accuracy of nine to ten significant figures with four or five evaluations of S-matrix element. Once $A_n(E_n)$ and E_n are known, the desired bound-free matrix elements are computed directly from Eq. (20). A simple shift of $E-E_n$ in the definition of the ϵ_a asymptotic energy guarantees that it is enough to solve Eq. (24) only once, i.e., that the value of $A_n(E_n)$ may be used for all energies [25].

An illustration of a typical basis set used in our computations, together with the hierarchy of interstate couplings, induced by V, is shown in Fig. 1. The illustration distinguishes between states, drawn with continuous line, used in the circular polarization calculations, and additional states, drawn with dotted line, needed for the linear polarization case. States with higher photon numbers than the initial number of photons (n_i) represent the counter-rotating terms. Their role is very similar to that of "closed" channels in ordinary nonradiative scattering.

III. RESULTS AND DISCUSSION

Before presenting the full hydrogenic ATI computations, we discuss two crucial tests of the methodology. The first deals with the convergence of the propagation in the radial distance R and the rate at which we need to switch off the laser field in order to attain stable results. The second is a test of the validity of the dipole approximation for very long-range interactions, such as those encountered in the present problem. These two tests are intimately connected, as they both deal with the fact that although the electron resides in a strong laser field which may extend over more than 10 000 bohrs, the range of effective interaction of the electron with the field is considerably smaller.

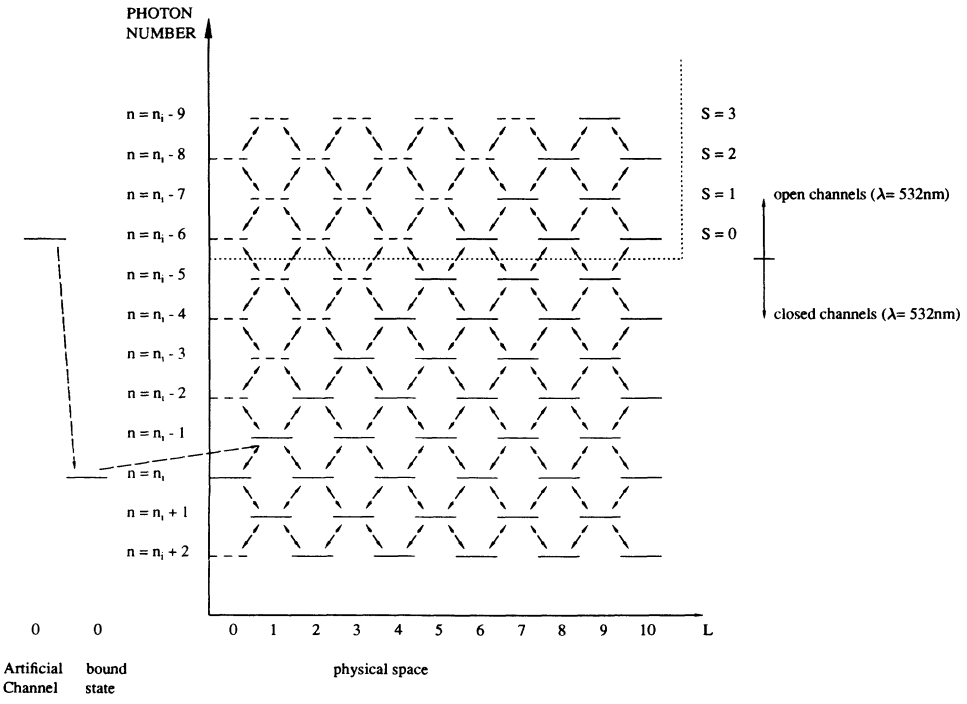

FIG. 1. Illustration of a typical basis set used in the CC expansion for six-photon ionization of hydrogen by circularly polarized light (solid lines) and linearly polarized light (solid and dotted lines). Note that this basis properly accounts for counterrotating terms.

TABLE I. Convergence of the computed ionization rates (in sec^{-1}) for the first three ATI peaks as a function of the laser spot-size parameter α of Eq. (12). The numbers in square brackets denote powers of 10.

α	$S=0$	$S=1$	$S=2$
30	2.2[+8]	9.45[+7]	2.40[+7]
50	3.7[+8]	1.20[+8]	1.48[+7]
70	4.2[+8]	1.35[+8]	1.33[+7]
100	4.5[+8]	1.27[+8]	1.28[+7]
181	4.7[+8]	1.29[+8]	1.26[+7]
201	4.8[+8]	1.30[+8]	1.26[+7]
301	4.9[+8]	1.33[+8]	1.28[+7]
402	5.0[+8]	1.33[+8]	1.28[+7]
804	5.0[+8]	1.33[+8]	1.28[+7]

The range of the R propagation is a strong function of the laser spatial extension and its intensity, since ideally it must be continued until the laser field is negligible. It turns out that the S matrix becomes constant at much smaller distances if a gradual switch-off of the laser field is introduced. Without such switch-off, the S matrix is expected [32] to oscillate with R, roughly as $\exp(i\omega^{3/2}m_e R^2/\{4[\hbar E(l+1)]^{1/2}\})$.

A study of the effects of the laser switch-off is given in Table I. We find that although convergence (with respect to R and with respect to the number of channels) is slower with increase in the laser spot size, for a given intensity the ATI rates and angular distribution cease to change beyond a certain spot-size value. The reason for this behavior may be gleaned from Fig. 2, where we plot a $\langle n_i-1|\langle 1,0|V|0,0\rangle|n_i\rangle$ interaction matrix element for five laser profiles (different $\mathcal{U}$ functions) of the *same* intensity. We display the *complete* interaction matrix element [derived from Eq. (11)], and its dipolar portion, obtained by maintaining the first term in the Taylor expansion of the $\exp\{\pm i\mathbf{k}\cdot\mathbf{R}\}$ factor of Eq. (11).

It is clear from Fig. 2 and especially from Fig. 2(f), where the potentials for all five laser widths are lumped together, that given a distance R_f, an additional increase beyond a certain value $\alpha_{\min}$ of the range of the $\mathcal{U}$ function leaves the interaction matrix element for $R<R_f$ un-

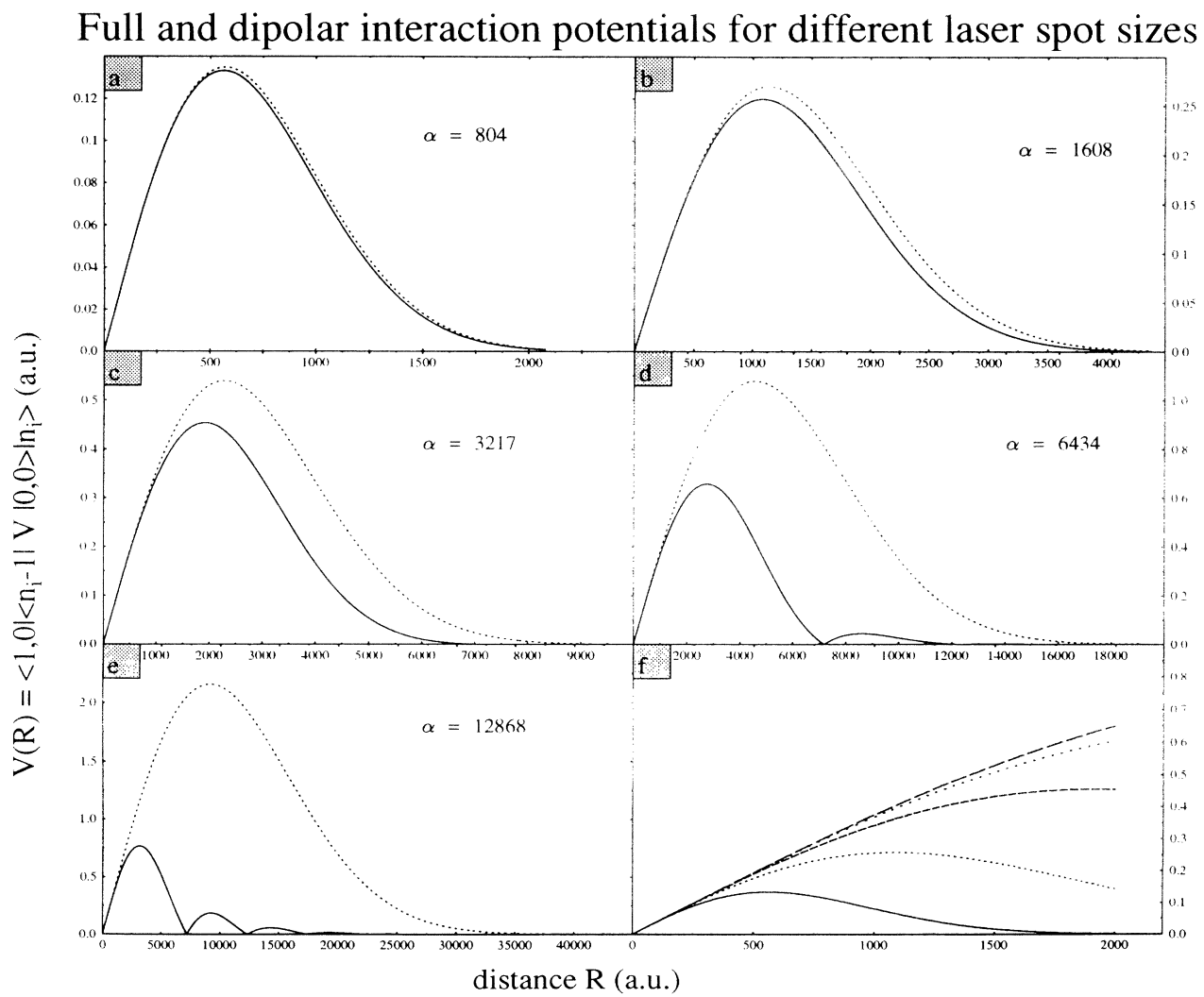

FIG. 2. Comparison of the full (solid line) and dipolar (dotted line) field-matter interaction potential as a function of R for five different laser spots sizes. Plotted is $V(R)=\langle 1,0|\langle n_i-1|V|0,0\rangle|n_i\rangle$. (f) displays a summary of the full field-matter interaction potentials of Figs. 2(a)–2(e) as a function of the laser spot size.

changed. For example, for $R_f = 180$ a.u. the above holds true for all $\alpha \geq \alpha_{\min} = 804$ a.u. For $R_f = 760$ a.u. the interaction matrix element are the same for $\alpha \geq \alpha_{\min} = 3217$ a.u. If, in addition, $R_f = R_{\text{free}}$, a distance beyond which the continuum electron is "free," i.e., it does not absorb or emit photons [33], then it follows from the above that differences in the laser spatial profile for $R > R_f$ do not influence the final electron distribution.

We can use this argument to estimate R_{free}: Since the ATI spectrum is independent of the laser width for widths greater than a minimal one, $\alpha > \alpha_{\min}$, we can use a series of calculations of decreasing widths to find the minimal value for which the ATI spectrum is unchanged. By plotting the interaction matrix elements for this series, as done in Fig. 2(f) we can estimate R_{free} as the R value at which the minimal-width curve begins to deviate from the larger-width curves. For example, for $\lambda = 532$ nm and $I = 1 \times 10^{13}$ W/cm^2 we obtain $\alpha_{\min} \approx 200$ a.u. and $R_{\text{free}} \approx 40$ a.u.

Because we have found the electron to be free at much smaller distances than the laser spot size, we also have good reason to believe that the dipole approximation may be valid for ATI calculation despite the strong interaction and the large distances involved. This has been implicitly assumed in past calculations but never really tested. Our present method enabled us to check this point by including the full form of the field (which involves therefore higher multipolar transitions).

In Table II we compare the ATI rates obtained from the full potential and the dipole approximation for $\lambda = 265$ nm and $I = 6.4 \times 10^9$ W/cm^2. We see that the dipole approximation yields essentially the same ATI rates as the full-interaction form [34].

We now turn our attention to the hydrogenic ATI problem. We first look at the angular distribution of the ATI electrons for both linear and circular polarization. In circular polarization, only one angular-momentum state ("partial wave"), which is equal to its z-axis projection, may result from an N photon absorption process. Hence, irrespective of the intensity, the angular distribution is proportional to $|Y_{M,M}(\theta_c)|^2 \sim \sin^{2M}\theta_c$, where θ_c is the angle between the propagation direction of the light and the direction of the ejected electron, $M = N + M_i$, with M_i being the z-projection of the initial angular momentum of the electron. In contrast, in the linear-polarization case, a number of partial waves, whose coefficients are intensity dependent, contribute to each ATI peak. As a result, the angular distribution (which is

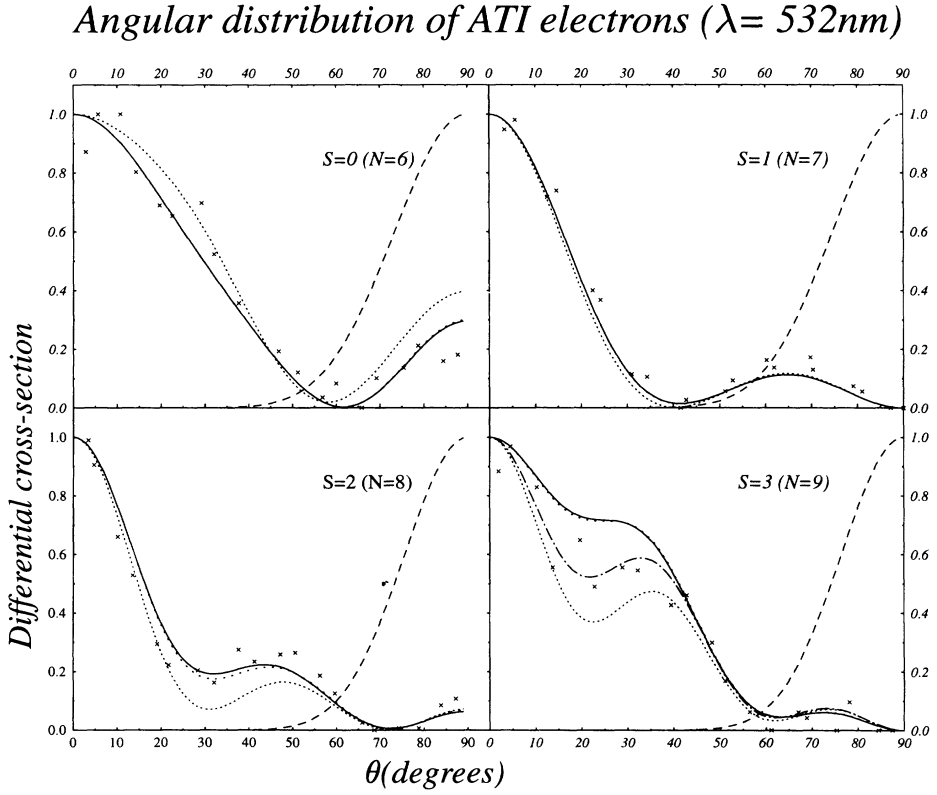

FIG. 3. The electronic angular distributions of hydrogen initially in the 1s state, ionized by linearly and circularly polarized 532-nm light, at different kinetic-energy peaks. θ is the angle between the direction of polarization of the field and the ejected electron for linear polarization and the angle between the propagation direction of the light and the ejected electron for circular polarization. S denotes the ATI peak, that is, the number of extra photons (over the minimum require for ionization) absorbed in the continuum. (— — —): the circular distribution; (× × ×): experimental results of Ref. [21] with zero-line subtraction; (——): perturbative calculations of Ref. [7]; (- - - -): present weak-intensity calculations $I = 6.4 \times 10^{10}$ W/cm^2 (our weak intensity and the perturbative calculations are almost indistinguishable from one another); (· · · ·): present high-intensity calculations $I = 1.6 \times 10^{13}$ W/cm^2; (—·—·—·): for $S = 3$ the curve $I = 6.4 \times 10^{12}$ W/cm^2 is also plotted.

TABLE II. Comparison of the ionization rates (in sec^{-1}) for the first four ATI peaks obtained for the full-interaction potential, and the dipole approximation for circularly polarized light at $\lambda=265$ nm and $I=6.4\times10^{9}$ W/cm^2. The numbers in square brackets denote powers of 10.

	Dipole potential			Full potential		
ATI peak	$\alpha=201$	$\alpha=1608$	$\alpha=5025$	$\alpha=201$	$\alpha=1608$	$\alpha=5025$
$S=3$	3.40[−15]	3.30[−15]	3.27[−15]	3.40[−15]	3.30[−15]	not converged
$S=2$	8.20[−10]	8.13[−10]	8.13[−10]	8.20[−10]	8.16[−10]	not converged
$S=1$	1.31[−4]	1.32[−4]	1.32[−4]	1.31[−4]	1.32[−4]	not converged
$S=0$	7.20[0]	7.27[0]	7.27[0]	7.17[0]	7.27[0]	7.28[0]

now a function of θ_l, the angle between the field polarization direction and that of the ejected electron) does change with intensity.

In Fig. 3 we display the angular distribution for the first four linearly polarized ATI peaks (denoted $S=0,1,2,3$). For comparison, we also include the circular-polarization angular distribution. Linear-polarization calculations for both "weak" ($I=6.4\times10^{10}$ W/cm^2) and "strong" illuminations ($I=1.6\times10^{13}$ W/cm^2) are presented. These calculations are contrasted with the perturbation results of Gontier, Rahmin, and Trahin [7] and with the (background-subtracted) experimental results of Wolff *et al.* [21].

As shown in Fig. 3, at high intensities our results deviate substantially from the perturbative results, whereas in the weak-field regime both sets of calculations agree very well. The failure of perturbation theory is especially noticeable for the highest ($S=3$) ATI peak. For this peak, our results, contrary to the perturbative calculations, fit the (background-subtracted) experimental points quite well [35].

In Figs. 4 (displaying the $S=2$ peak) and 5 (displaying the $S=3$ peak) we study the dependence of the angular and partial-wave distributions on intensity. We see that the angular distributions become more peaked as we raise the intensity. This is explained by the reduction in the contribution of the lower partial waves ($l=0$ and 2 for $S=2$, and $l=1$ and 3 for $S=3$) with intensity. Since the higher partial waves are cut off from above , at $l>4$ (for $S=2$) and $l>5$ (for $S=3$) at *all* intensities, the angular distribution is dominated more and more by the highest present ($l=4$ for $S=2$ and $l=5$ for $S=3$) partial wave.

The integral cw ionization rates to different final kinetic-energy states at $\lambda=532$ nm, are given in Fig. 6

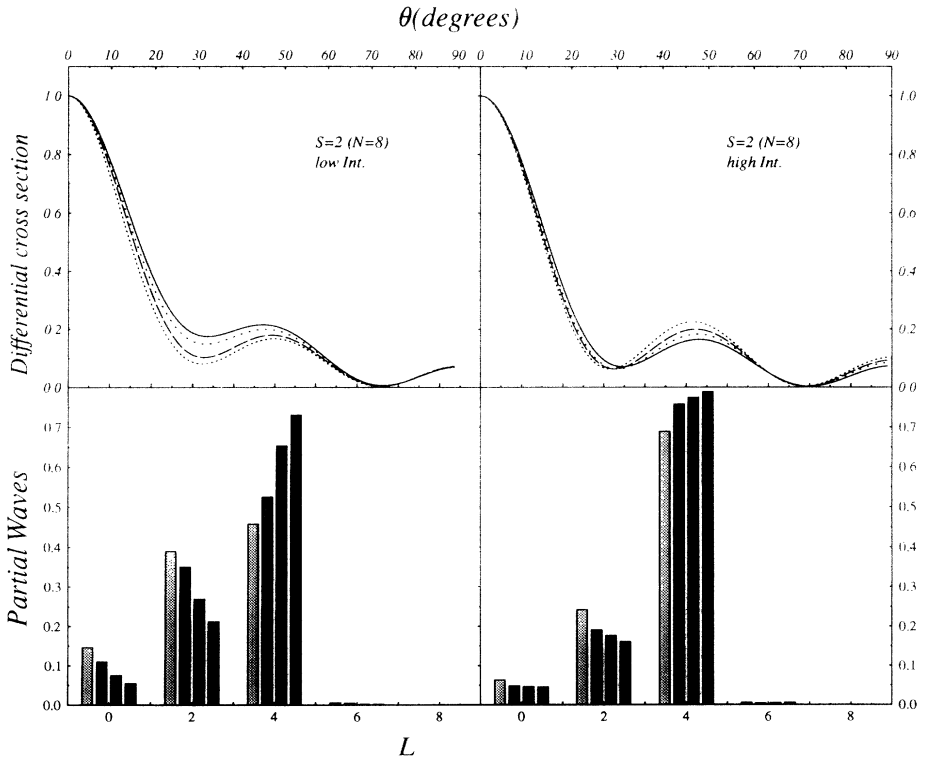

FIG. 4. Angular distribution and partial wave histograms of the $S=2$ peak at several intensities. Low intensities: (——): $I=6.4\times10^{10}$ W/cm^2, (- - - -): $I=1.9\times10^{12}$ W/cm^2, (— — —): $I=6.4\times10^{12}$ W/cm^2, (· · · ·): $I=1.0\times10^{13}$ W/cm^2. High intensities: (——): $I=10^{13}$ W/cm^2, (- - - -): $I=1.6\times10^{13}$ W/cm^2, (— — —): $I=1.8\times10^{13}$ W/cm^2, (· · · ·): $I=2.0\times10^{13}$ W/cm^2. The histograms are ordered from left to right with increasing intensities.

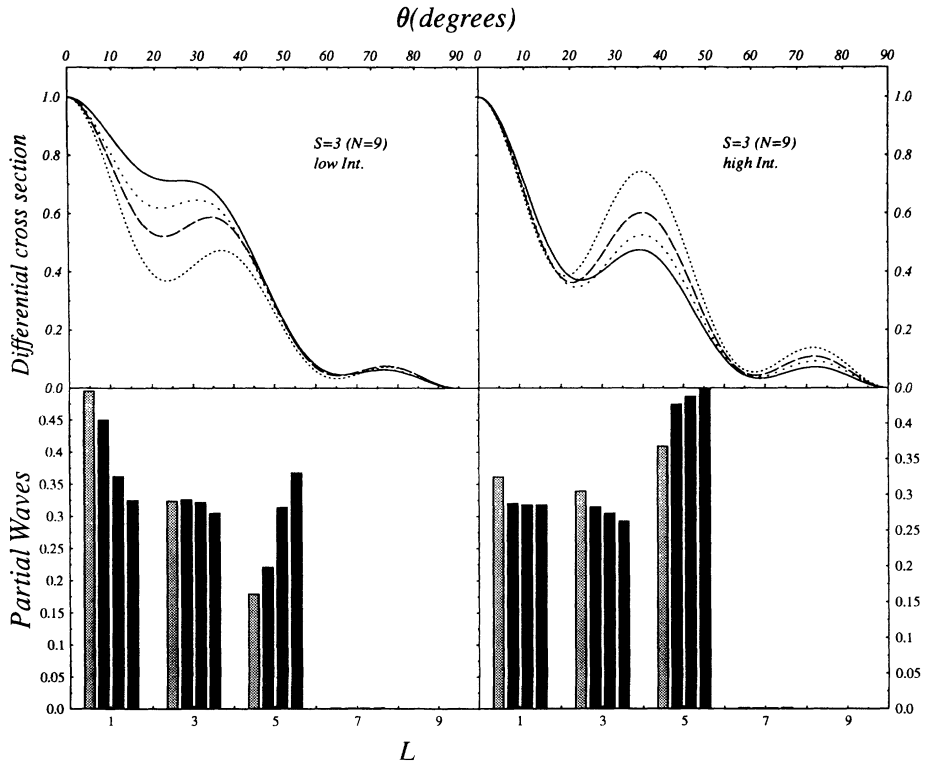

FIG. 5. The same as in Fig. 4, for $S=3$ peak.

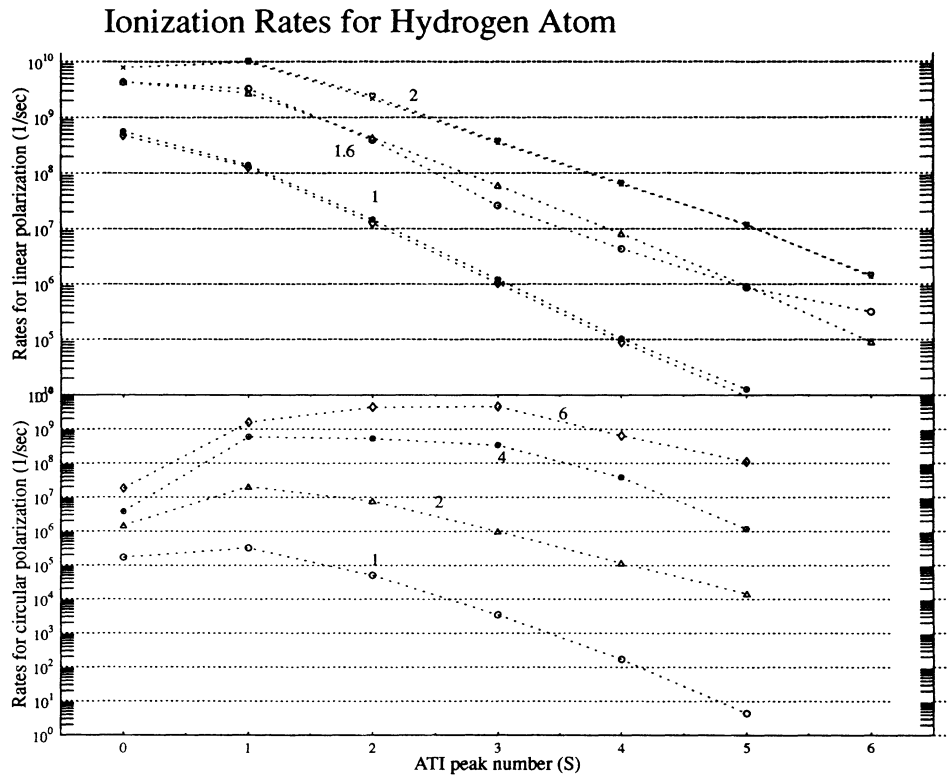

FIG. 6. Partial ATI ionization rates for different ATI peaks at $\lambda=532$ nm for both linear (upper figure) and circular (lower figure) polarizations. S denotes the ATI peak, that is, the number of extra photons (over the minimum require for ionization) absorbed in the continuum. Linear polarization: $I=10^{13}$ W/cm^2: ($\oplus$), our calculations, ($\Diamond$), computational results of Ref. [19] (almost indistinguishable from ours); $I=1.6\times10^{13}$ W/cm^2: (Δ), our calculations, ($\circ$), experimental results of Ref. [21]; $I=2.0\times10^{13}$ W/cm^2: ($\times$), our calculations, ($\heartsuit$), computational results of Ref. [19]. Circular polarization (present results): ($\circ$), $I=1.0\times10^{13}$ W/cm^2, (Δ), $I=2.0\times10^{13}$ W/cm^2, ($\oplus$), $I=4.0\times10^{13}$ W/cm^2, ($\Diamond$), $I=6.0\times10^{13}$ W/cm^2.

for both linear and circular polarizations. The linear polarization results are contrasted with the short-pulse results of Schafer and Kulander [19] and with the experimental measurements of Wolff *et al.* [21]. Clearly, in the linear-polarization case, there is excellent agreement between our cw results and the short-pulse results. Apparently, at intensities as high as 10^{13} W/cm^2 the pulsed ATI ionization rate reaches a steady state early on in the history of the pulse and the pulsed calculations essentially yield the steady-state rate. The comparison with the experiment (where a nanosecond pulse laser was used) is also quite satisfactory, considering the uncertainty in the experimental intensities.

For circular polarization (at $\lambda=532$ nm) there are no nonperturbative calculations to compare with. Neither are there any quantitative experimental results for hydrogen, as Wolff *et al.* [21] reported zero signal in this case. This finding actually correlates well with the computations shown in Fig. 6, where the circular-polarization cross sections at four different intensities ($I=1.0$, 2.0, 4.0, and 6.0×10^{13} W/cm^2) are contrasted with the linear-polarization ones. Typically, the circular polarization cross sections are three orders of magnitude weaker than the linear ones. This explains well why circular-polarization ATI was much harder to detect.

Figure 6 also displays quantitatively the "peak-suppression" effect, which is the tendency of the ATI electrons to peak at kinetic-energy values well above the threshold for ionization. We show in Fig. 6, in good agreement with experiments on other systems [36], that peak suppression is more pronounced in circularly polarized ATI as compared to ATI with linearly polarized light. Thus, the suppression of the first peak ($S=0$) in the circular-polarization case is already observed at $I=1\times10^{13}$ W/cm^2, whereas for linear polarization the same effect is observed only at $I=1.6-2.0\times10^{13}$ W/cm^2.

The usual explanation given to the peak-suppression effect [36] asserts that the nearly free electron acquires from the field an average ponderomotive potential,

$$U_p=\tfrac{1}{2}m\langle\dot{r}^2\rangle=\frac{e^2\overline{\mathcal{E}}^2}{2m\omega^2} \tag{25}$$

where m is the electron's mass, c is the speed of light, and $\overline{\mathcal{E}}^2$ denotes an average over the square of the electric field. The ponderomotive potential, which is slowly converted to kinetic energy as the electron exits the field, is the minimal kinetic energy at which we can observe the electron. The larger the ponderomotive potential, the larger the peak-suppression effect.

Equation (25) is consistent with the results of Fig. 6 only if the ponderomotive potential experienced in the circular polarization case is substantially larger than that of a linearly polarized field of the same intensity. A simple averaging of the field squared, however, fails to yield this effect. Specifically, in the case of linear polarization we have that

$$U_{\rm lin}=\frac{e^2\mathcal{E}_0^2\overline{\sin^2\omega t}}{2m\omega^2}=\frac{e^2\mathcal{E}_0^2}{4m\omega^2}\ , \tag{26}$$

where $\mathcal{E}_0$ is the electric-field amplitude. For circular polarization we obtain from the field's two out-of-phase contributions (the x and y components) that

$$U_{\rm circ}=\frac{e^2\mathcal{E}_0^2}{4m\omega^2}\{\sin^2\omega t+\sin^2(\omega t+\pi/2)\}=\frac{e^2\mathcal{E}_0^2}{4m\omega^2}\ , \tag{27}$$

We see that the above procedure yields the same average ponderomotive potential for both types of polarizations. Note that in Eq. (27) we have accounted for the fact that the x or y field amplitude of a circularly polarized light is $1/\sqrt{2}$ the amplitude of a linearly polarized beam of the same intensity.

The simple averaging over the field squared fails because it does not take into account the fact that the ponderomotive potential is acquired mainly when the electron is near the proton and not when it is completely free. In order to remedy that we must allow both the electron and the proton to be involved in the process and allow the proton to recoil in the opposite direction to the momentum acquired (lost) by the electron upon absorption (emission) of a photon. We therefore switch to center-of-mass coordinates and replace $\dot{r}$ in Eq. (25) by the e-p relative velocity $\dot{r}_{e\text{-}p}$ and m by m_e, the electron-proton reduced mass. We obtain that

$$U_p=\tfrac{1}{2}m_e\langle\dot{r}_{e\text{-}p}^2\rangle=\frac{e^2\overline{\mathcal{E}}_r^2}{2m_e\omega^2}\ , \tag{28}$$

where $\mathcal{E}_r$ is the projection of the field on the electron-proton relative direction.

This seemingly small change has far-reaching consequences regarding the electronic kinetic-energy distribution. What enters Eq. (28) is not just the field, but the field projected on the instantaneous dipole created by the electron and the proton. As we show below, the projection of the field "experienced" by the electron as it is being ejected is quite different in the two polarization cases.

A glance at the different angular distributions of the ejected electron, shown in Figs. 3–5, makes clear why this is so. As shown in Fig. 3, in the circular case the electronic angular distribution is peaked perpendicular to the propagation direction, i.e., the ejected electron moves always in the plane of the field. This effect increases as the electron absorbs more and more photons because the angular distribution, is proportional to $\sin^{2M}\theta_c$ ($M=N+M_i$ with N being the number of photons absorbed), which becomes narrower with increasing N.

In the linear case the electronic angular distribution is much broader as it is described by a sum of $P_L(\cos\theta_l)$ partial waves. In fact, as shown in Figs. 4 and 5, at high intensities the angular distribution tends to move away from the $\theta_l=0$ direction. For those electrons exiting in directions other than the field direction, the projection of the field on the instantaneous dipole can be quite small, and the ponderomotive potential accordingly small.

In order to see this more quantitatively we have computed the ponderomotive potential in Eq. (28) by calculating the angular averages of $\mathcal{E}_r^2$ using the actual angular distributions of Figs. 3–5. We obtain that the value $U_p=2\pi e^2I/m_ec\omega^2$ ($=9.719\times10^{-3}$ a.u. for $\hbar\omega=2.33$ eV

TABLE III. Linear x_l and circular x_c angular factors of the ponderomotive potential obtained from the angular distributions of Fig. 3 for $I=6.5\times10^{10}$ W/cm^2, $I=10^{13}$ W/cm^2, and $I=1.6\times10^{13}$ W/cm^2.

Polarization	$S=0$	$S=1$	$S=2$	$S=3$
Circular	0.933	0.941	0.947	0.952
Linear $I=6.5(10)$	0.547	0.605	0.607	0.657
Linear $I=1.0(13)$	0.498	0.590	0.596	0.621
Linear $I=1.6(13)$	0.474	0.572	0.575	0.600

and $I=1.0\times10^{13}$ W/cm^2) must be corrected by multiplying it with

$$x_l=\int\cos^2\theta D_l(\theta)\sin\theta d\theta \tag{29}$$

for linear polarization, and by

$$x_c=\int\sin^2\theta D_c(\theta)\sin\theta d\theta \tag{30}$$

for the circular-polarization case. In the above, $D_{l(c)}$ is the normalized angular distribution for the linear (circular) polarization.

As shown in Table III the ponderomotive potential in the circular polarization case is substantially higher than that of the linear polarization case, with the gap widening as we increase the intensity. In order to illustrate the role of the ponderomotive potential we compute the energetic requirements for a six-photon absorption process. An electron assumed to be initially in the ground state, with energy E_0 ($E_0=-\frac{1}{2}$ a.u.), acquires, after absorbing six photons, the following energy

$$E=6\hbar\omega-E_0=1.376\times10^{-2}\text{ a.u.} \tag{31}$$

It follows from Table III that this energy is almost three times the ponderomotive potential at $I=10^{13}$ W/cm^2 for linear polarization ($U_{\rm lin}=0.498\times U_p=4.84\times10^{-3}$ a.u.) and only 40% higher than the ponderomotive potential for the circular case ($U_{\rm circ}=0.933\times U_p=9.10\times10^{-3}$ W/cm^2). Consequently, as shown in Fig. 6, the first ATI peak is suppressed in the circular case, whereas no such effect is seen in the linear case.

IV. CONCLUSIONS

We have presented a method based on the ACM for computing ATI with cw light. The method bypasses the need to calculate (bound or scattering) wave functions as it yields directly the relevant bound-free matrix elements. Moreover, the whole ATI process including the passage from the bound manifold to the continuum and the subsequent excitation in the continuum, is treated uniformly by a single set of equations. In this way we can carry out computations for off-resonant as well as resonantly aided [37] processes.

We have applied this method to the 3D ATI of hydrogen in intense laser fields. We have computed the ionization rates, the kinetic-energy distribution, and the angular distributions of the photoelectrons for different ATI peaks. We have presented computations for light intensities varying over four orders of magnitude, for circular, as well as linear, polarizations. We find the circular-polarization cross sections to be three orders of magnitude weaker than the corresponding linear ones and that peak suppression is more extensive for circular polarization. This last effect is explained quantitatively as due to the difference in the angular distribution of the ejected electron in these two cases. In so doing we have shown why the ponderomotive potential is greater for circular polarization than for linear polarization. We conclude that the 3D aspects of the process and, explicitly, the angular-momentum constraints imposed by absorption of linearly or circularly polarized photons determine to a large extent the kinetic-energy distribution of the photoelectrons.

[1] L. V. Keldish, Zh. Eksp. Teor. Fiz. **47**, 1945 (1964) [Soviet Phys. JETP **20**, 1307 (1965)].
[2] F. H. Faisal, J. Phys. B **6**, L312 (1973).
[3] H. R. Reiss, J. Phys. B **20**, L79 (1987).
[4] P. B. Corkum, N. H. Burnett, and F. Brumel, Phys. Rev. Lett. **62**, 1259 (1989).
[5] G. Petite, P. Agostini, and H. G. Muller, J. Phys. B **21**, 4097 (1988).
[6] J. Javanainen and J. H. Eberly, J. Phys. B **21**, L93 (1988).
[7] Y. Gontier, N. K. Rahman, and M. Trahin, Europhys. Lett. **5**, 595 (1988).
[8] G. Kracke, H. Marxer, J. T. Broad, and J. S. Briggs, Z. Phys. D **8**, 103 (1988).
[9] M. Crance and M. Aymar, J. Phys. B **13**, L421 (1980).
[10] Z. Deng and J. H. Eberly, Phys. Rev. Lett. **53**, 1810 (1984).
[11] K. Rzazewski and R. Grobe, Phys. Rev. A **33**, 1855 (1986).
[12] M. Trippenbach, K. Rzazewski, and R. Grobe, Phys. Rev. A **37**, 4194 (1988).
[13] M. Dorr and R. Shakeshaft, Phys. Rev. A **38**, 543 (1988).
[14] J. Javanainen, Q. Su, and J. H. Eberly, Phys. Rev. A **38**, 3430 (1988).
[15] C. Cerjen and R. Kosloff, J. Phys. B **20**, 4441 (1987).
[16] S. M. Susskind and R. V. Jensen, Phys. Rev. A **38**, 132 (1988).
[17] K. C. Kulander, Phys. Rev. A **35**, 445 (1987).
[18] S.-I. Chu and J. Cooper, Phys. Rev. A **32**, 2769 (1985).
[19] K. J. Schafer and K. C. Kulander, Phys. Rev. A **42**, 5794 (1990).
[20] P. H. Bucksbaum, R. R. Freeman, M. Bashkansky, and T. McIlrath, J. Opt. Soc. Am. B **4**, 760 (1987).
[21] B. Wolff, H. Rottke, D. Feldman, and K. H. Welge, Z. Phys. D **10**, 35 (1988).
[22] S.-I. Chu and R. Yin, J. Opt. Soc. Am. B **4**, 720 (1987).
[23] R. M. Potvliege and R. Shakeshaft, Phys. Rev. A **41**, 1609 (1990).
[24] M. Dorr, P. G. Burke, C. J. Joachin, C. J. Noble, J. Purvis, and M. Terso-Dunseath, J. Phys. B **26**, L275

(1993).
[25] M. Shapiro, J. Chem. Phys. **56**, 2582 (1972); M. Shapiro and R. Bersohn, Ann. Rev. Phys. Chem. **33**, 409 (1982).
[26] G. G. Balint-Kurti and M. Shapiro, Adv. Chem. Phys. **60**, 403 (1985).
[27] D. E. Manolopoulus, J. Chem. Phys. **85**, 6425 (1986).
[28] B. R. Johnson, J. Comput. Phys. **13**, 445 (1973).
[29] The only limitation on our choice of these potentials is imposed by the requirement that the artifical wave function F_a serve as an effective soure term. This requirement is satisfied by insuring nonnegligible spatial overlap between the artifical wave function and the bound manifold coupled to it.
[30] M. Shapiro and G. G. Balint-Kurti, J. Chem. Phys. **71**, 1461 (1978).
[31] G. G. Balint-Kurti, R. E. Moss, I. A. Sadler, and M. Shapiro, Phys. Rev. A **41**, 4913 (1990).
[32] This can be shown using the distorted-wave Born approximation and the stationary-phase approximation for the radial integrals.
[33] Absorption or emision of a photon takes place through the Coulomb interaction, which allows for momentum transfer to the proton, thus compensating for the extra momentum given to the system by the photon.
[34] At bigger spot sizes our full-interaction calculations did not converge with respect to the number of channels, since we were limited by the memory size of our RS/6000/320H work station. At these spot sizes the reliability of the dipole approximation cannot be guaranteed.
[35] There are experimental uncertainties in the intensity which make the exact comparison difficult. Wolff *et al.* [21] estimate that $I \approx 6 \times 10^{12}$ W/cm^2 for the $S=0$ measurements and $I \approx 1.6 \times 10^{13}$ W/cm^2 for $S=1,2,3$ measurements, with the uncertainty in the $S=0$ measurement being greater than that of $S=1,2$, and 3 measurements.
[36] G. Petite, P. Agostini, and F. Yergeau, J. Opt. Soc. Am. B **4**, 765 (1987); P. H. Bucksbaum, M. Bashkansky, R. R. Freeman, T. McIlrath, and L. F. DiMauro, Phys. Rev. Lett. **56**, 2590 (1986); P. B. Corkum, N. H. Burnett, and F. Brumel, Phys. Rev. Lett. **62**, 1259 (1989).
[37] R. Blank and M. Shapiro (unpublished).

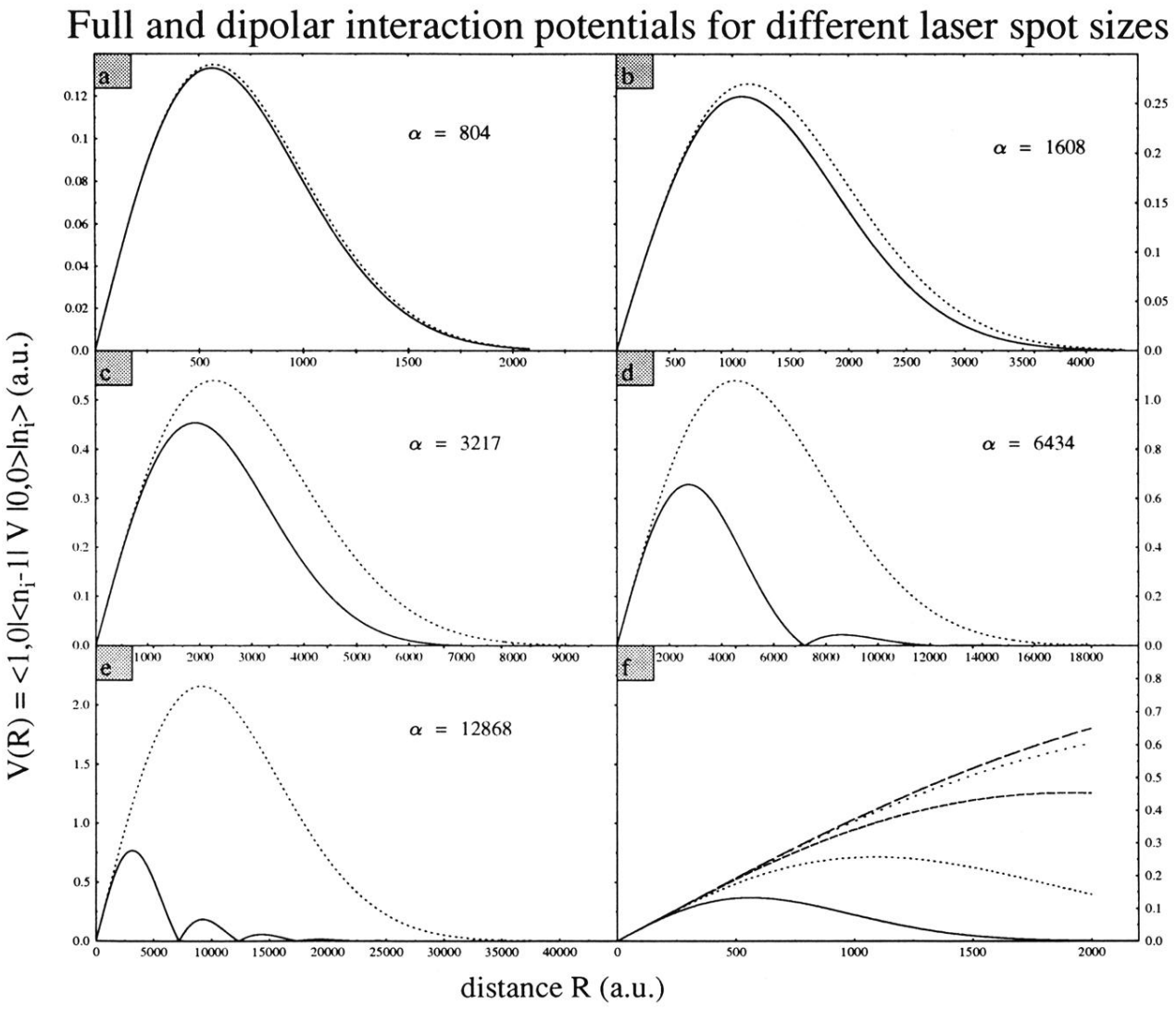

FIG. 2. Comparison of the full (solid line) and dipolar (dotted line) field-matter interaction potential as a function of R for five different laser spots sizes. Plotted is $V(R) = \langle 1,0|\langle n_i - 1|V|0,0\rangle|n_i\rangle$. (f) displays a summary of the full field-matter interaction potentials of Figs. 2(a)–2(e) as a function of the laser spot size.

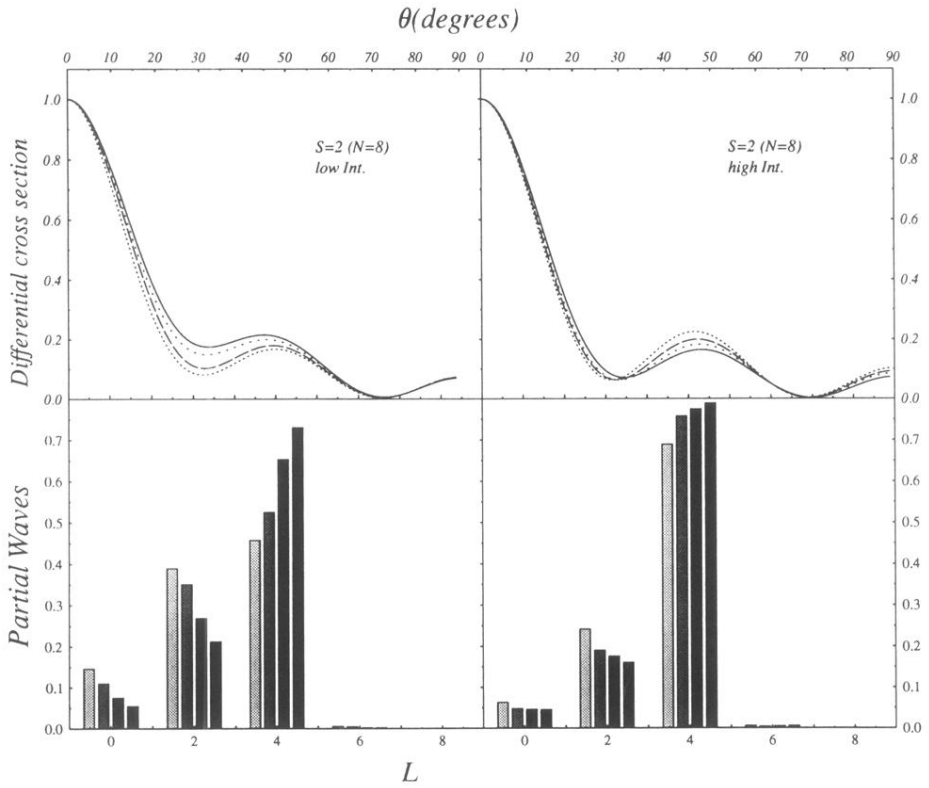

FIG. 4. Angular distribution and partial wave histograms of the $S=2$ peak at several intensities. Low intensities: (——): $I=6.4\times10^{10}$ W/cm^2, (- - - -): $I=1.9\times10^{12}$ W/cm^2, (— — —): $I=6.4\times10^{12}$ W/cm^2, (· · · ·): $I=1.0\times10^{13}$ W/cm^2. High intensities: (——): $I=10^{13}$ W/cm^2, (- - - -): $I=1.6\times10^{13}$ W/cm^2, (— — —): $I=1.8\times10^{13}$ W/cm^2, (· · · ·): $I=2.0\times10^{13}$ W/cm^2. The histograms are ordered from left to right with increasing intensities.

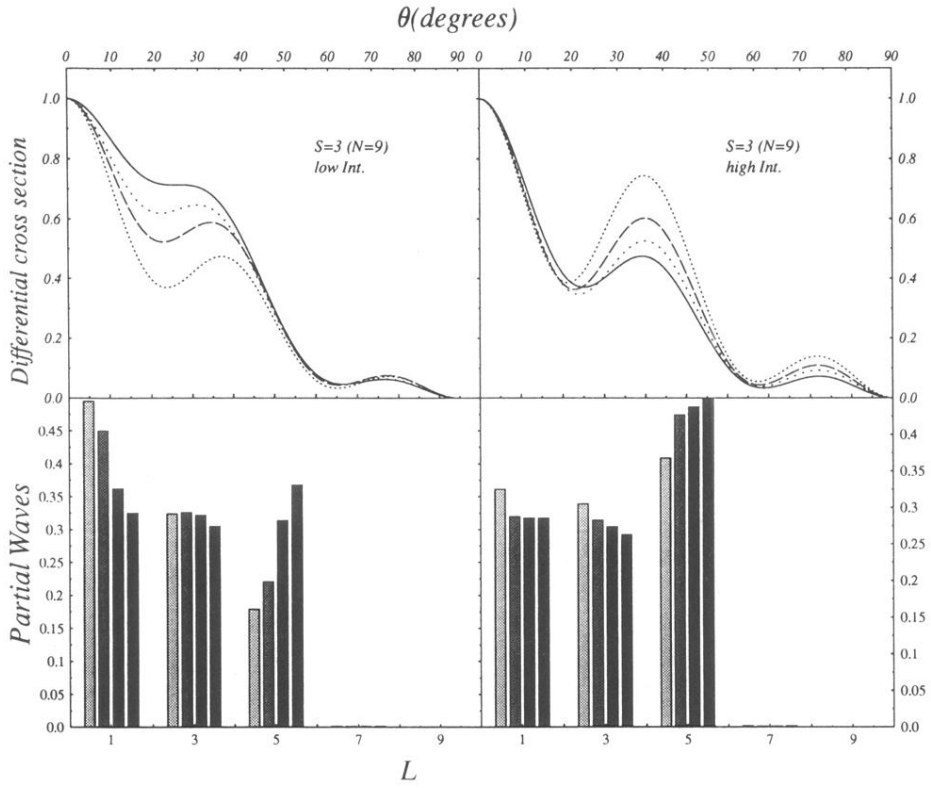

FIG. 5. The same as in Fig. 4, for $S=3$ peak.